Plasma Physics and Controlled Fusion

PAPER

Geometry dependence of the fluctuation intensity in gyrokinetic turbulence

To cite this article: G M Staebler *et al* 2021 *Plasma Phys. Control. Fusion* **63** 015013

IOP Publishing Plasma Physics and Controlled Fusion
Plasma Phys. Control. Fusion **63** (2021) 015013 (12pp) https://doi.org/10.1088/1361-6587/abc861

Geometry dependence of the fluctuation intensity in gyrokinetic turbulence

G M Staebler[1], J Candy[1], E A Belli[1], J E Kinsey[2], N Bonanomi[3] and B Patel[4,5]

[1] General Atomics, San Diego, CA, United States of America
[2] CompX, San Diego, CA, United States of America
[3] IPP, Garching, Germany
[4] CCFE, Culham, United Kingdom
[5] York Plasma Institute, University of York, York, United Kingdom

E-mail: Gary.Staebler@gat.com

Received 15 September 2020, revised 2 November 2020
Accepted for publication 6 November 2020
Published 27 November 2020

Abstract

The findings of an investigation into the properties of the three dimensional (3D) saturated fluctuation intensity of the electric potential in gyrokinetic turbulence simulations is presented. Scans in flux surface elongation and Shafranov shift are used to isolate the tokamak geometric dependencies. The potential intensity required in order to compute exact fluxes by a quasilinear method is determined using linear eigenmodes computed with the gyrokinetic code. A model of this non-linear intensity is constructed using the linear eigenmode properties and the geometry shape functions obtained from the 3D intensity spectrum. The model computes the poloidal wavenumber spectrum of the electron and ion energy fluxes with unprecedented accuracy. New insights are gained into the way zonal flow mixing saturates ion-scale turbulence by controlling the radial wavenumber width of the turbulence spectrum.

Keywords: tokamak transport, quasi-linear model, gyrokinetic turbulence

1. Introduction

Gaining an empirical understanding of turbulence by examining the properties of the spectra is not as daunting a task as it might seem. The goal is not to understand everything about the temporal and spatial behaviour of the turbulence. The goal of this study is just to model the electric potential (time dependent electrostatic potential) intensity required to compute the fluxes using the quasi-linear approximation (QL intensity) [1]. To be specific, the intensity of each poloidal wavenumber (k_y) required is the non-linear contribution to that wavenumber (Q_{k_y}) divided by the quasilinear weight of the most unstable linear eigenmode ($W^{QL}_{k_y}$) and the wavenumber spacing Δ_{k_y}

$$I^{QL}_{k_y} = \frac{Q_{ak_y}}{\Delta_{k_y} W^{QL}_{ak_y}}. \tag{1}$$

The quasi-linear weight is the formula for the non-linear flux (equation (2)) evaluated with just the most unstable linear eigenmode wavefunction (times a delta-function in k_x and k_y) and divided by the square amplitude (intensity) of the electric potential of that linear mode. The poloidal wavenumber grid interval Δ_{k_y} is needed in equation (1) to make the intensity independent of the k_y grid. It should not matter which plasma species (subscript label 'a') is used to compute this intensity, since the species dependence is accounted for in the quasi-linear weight. This is illustrated in figure 1 with an example from one of the simulations discussed later. All of the cases were found to give good agreement between the electron and ion calculations of the QL intensity. Using the same code to compute the linear eigenmodes, and the non-linear turbulence driven fluxes, eliminates the error due to approximated linear eigenmodes used in quasi-linear transport models like TGLF [2]. The saturation models used in TGLF prior to this paper were constructed based on the flux surface average potential intensity at $k_x = 0$, not the QL intensity as defined in equation (1). The gyro-Bohm normalized turbulent energy flux in the gyrokinetic simulation is computed for each species by the formula:

$$Q_a = \sum_{k_x}\sum_{k_y} \frac{3}{2}\langle \mathrm{Re}[ik_y \frac{ae\tilde{\phi}^*_{k_x,\,k_y}}{\rho_s T_e} \frac{a\tilde{p}_{a,\,k_x,\,k_y}}{\rho_s n_e T_e}]\rangle_{t,\theta} = \sum_{k_y} Q_{ak_y}. \tag{2}$$

Here the gyro-Bohm normalizations of the CGYRO code were used [3]: $c_s = \sqrt{T_e/m_D}$, $a =$ minor radius at separatrix, $\rho_s = c_s/\Omega_s$, $\Omega_s = eB_{\rm unit}/(m_D c)$, $B_{\rm unit} = \frac{qd\psi}{rdr}$ [4] for poloidal magnetic flux ψ, and $m_D =$ deuterium mass. The gyro-Bohm normalization for energy flux in these units is $n_e T_e c_s (\rho_s/a)^2$. The energy flux is produced by a radial $E \times B$ drift driven by electric potential fluctuations $\tilde{\phi}_{k_x,k_y}$ that is averaged with the fluctuations of the pressure moment of the species distribution function ($\tilde{p}_{a,k_x,k_y}$). The angle bracket represents a time average (t) and a flux surface average over a poloidal angle (θ). There is also a sum over the normalized radial wavenumber (k_x) which is equivalent to a radial average over the flux tube box. In this paper, we will be examining how the radial wavenumber and poloidal dependence of the time average electric potential intensity influence the QL intensity. Insights into the geometry dependence and the way in which the zonal ($k_y = 0$) potential fluctuations control the radial wavenumber width of the whole spectrum will be gained. A model for the QL intensity of unprecedented accuracy is constructed using these new results. This new model (SAT2) improves the ion-scale part of the model (SAT1) [5] that was developed to fit coupled electron-ion multi-scale gyrokinetic simulation spectra [6].

In section 2 the geometric metrics that make the wavevector coordinate independent and how these could impact the geometry dependence of the intensity will be discussed. In section 3 the intensity spectrum at the outboard midplane will be used to study the radial wavenumber width and its relation to the zonal potential fluctuations. In section 4 the poloidal dependence of the 3D spectrum will be studied. It will be shown that the wavenumber metrics can account for the poloidal dependence of the peak of the spectrum at $k_x = 0$. In section 5 a model for the QL intensity will be fit incorporating the radial wavenumber spectral width and flux surface average of the poloidally varying factors. The final section summarizes the paper and discusses the potential impact of this new SAT2 model on transport modeling of tokamaks and spherical tori.

2. Wavevector metrics in axisymmetric geometry

The geometric metrics that enter the gyrokinetic equation for general, axisymmetric, closed flux surface geometry will be shown in this paper to provide the functions that fit the poloidal dependence of the saturated potential intensity. The gyrokinetic equation is an approximation to the Vlasov–Fokker–Planck equation based on an expansion in the ratio of the magnetic gyroradius (Lamour radius) to the local equilibrium gradient length. This is a very small parameter in tokamaks and spherical tori with magnetic fields greater than one Tesla typical of todays fusion energy experiments. Because the gyroradius sets the scale for the plasma turbulence described by gyrokinetics, the wavelength perpendicular to the magnetic field is much shorter than the wavelength parallel to the magnetic field. This property makes it convenient to introduce an eikonal approximation for the perpendicular wavevector. The gradient of the eikonal (S) is perpendicular to the magnetic field vector **B**: $\mathbf{B} \cdot \nabla S = 0$. There are two independent functions that satisfy this constraint. An arbitrary function of the poloidal flux $S = S_x(\psi)$ and $S = n\left[\varphi + S_y\right]$ where n is a toroidal Fourier mode index and,

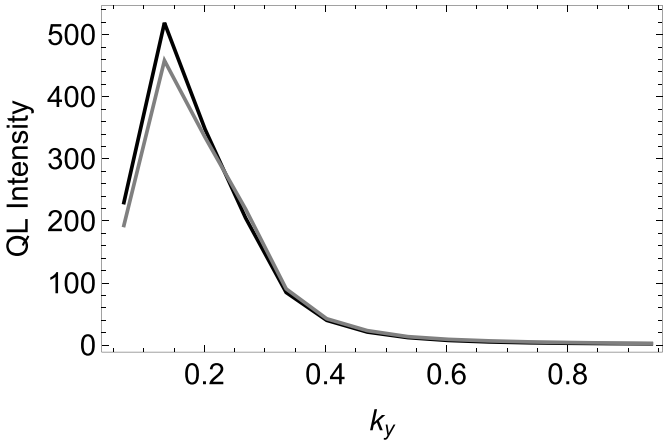

Figure 1. The QL intensity computed from the ion (black) and electron (gray) energy flux for the GA-STD case.

$$S_y = -\int_0^\theta d\theta' \frac{B_T}{R\mathbf{B_p}\cdot\nabla\theta'}. \tag{3}$$

Here a cylindrical coordinate system (R, φ, Z) is assumed and the magnetic field has toroidal $\mathbf{B}_T = I_T(\psi)\nabla\varphi$ and poloidal $\mathbf{B_p} = \nabla\varphi \times \nabla\psi$ components. The Miller geometry coordinates [7], minor radius and poloidal angle (r, θ), have been used for S_y. The eikonal function S_y is quasi-periodic with $S_y(\theta = 2\pi) = 2\pi q$ where q is the safety factor of the flux surface. An average over the fast motion about the magnetic field is taken in the gyrokinetic approximation. This results in Bessel functions with an argument $\left|\nabla S\right| v_\perp m_a c/(Z_a eB)$. This motivates defining a poloidally varying ion wavevector given by:

$$K_{i\perp}^2 = \rho_{iB}^2\left|\nabla S\right|^2 = \left[K_{iy}^2 + \left(\hat{s}K_{iy}\Theta + K_{ix}\right)^2\right], \tag{4}$$

where $\rho_{iB} = \sqrt{2T_i/m_i}/\Omega_B$, $\Omega_B = \frac{Z_i eB}{m_i c}$ are a gyro-radius and gyro-frequency using the ion temperature, mass and charge (T_i, m_i, Z_i) and using the total magnetic field magnitude $B(\theta)$. The magnetic shear is $\hat{s} = (r/q)\mathrm{d}q/\mathrm{d}r$. The generalized angle Θ in equation (4) is defined to be zero at the outboard midplane and has a quasi-periodic property derived from S_y. The poloidal K_{iy} and radial K_{ix} wavenumber components in equation (4) are defined by:

$$K_{iy}(\theta) = \frac{n\rho_{iB_p}}{R} = \frac{k_y\alpha_i}{|\nabla r|}, \tag{5}$$

$$K_{ix}(\theta) = |\nabla r|k_r\rho_{iB} = \frac{k_x\alpha_i}{G_q}\frac{B_{\rm norm}}{B_{\rm unit}}, \tag{6}$$

where the factor $\alpha_i = Z_{\rm norm}\sqrt{m_i 2T_i}/(Z_i\sqrt{m_{\rm norm}T_{\rm norm}})$ converts from the arbitrary external normalizations used in $\mathrm{k_x}$, k_y $(Z_{\rm norm}, m_{\rm norm}, T_{\rm norm})$ to the ion values. The flux surface shape

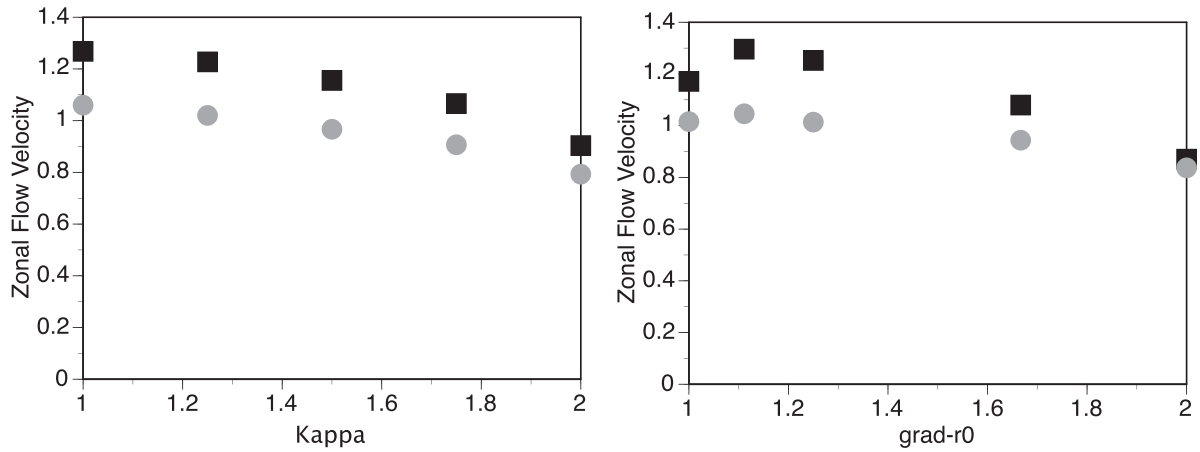

Figure 2. The zonal flow velocity computed from the potential spectrum equation (14) (black, box) and from the zonal flow mixing rule equation (13) (gray, circle) for elongation (κ) (left) and Shafranov shift (Δ) (right) scans. note: gradr0 $= |\nabla r|_0 = 1/(1+\Delta)$.

factor G_q has been introduced to make the distinction between the arbitrary normalizing magnetic field $B_{\rm norm}$ and $B_{\rm unit}$, which appears in the metric coefficients, clear.

$$G_q = \frac{rB}{qRB_p} = \frac{B}{B_{\rm unit}|\nabla r|}. \tag{7}$$

This shape factor reduces to 1 for a large aspect ratio circular flux surface. It is the same for GENE [8] or CGYRO since it does not involve the choice of normalizing magnetic field. The poloidal wavenumber K_{iy} (equation (5)) is the toroidal wavenumber n/R normalized by the ion gyroradius with respect to the poloidal magnetic field $\rho_{iB_p} = \rho_{iB}B/B_p$. The radial ion wavenumber K_{ix} (equation (6)) is the gradient normal to flux surfaces ($|\nabla r|k_r = |\nabla S_x|$) normalized to the the total magnetic field ion gyro-radius. The relation of these geometric wavenumbers to the externally normalized wavevectors k_y, and $k_x = k_r\rho_{B_{\rm norm}}$ is also given in equations (5) and (6). The CGYRO code uses the normalizing magnetic field $B_{\rm norm} = B_{\rm unit}$. The GENE code [8] uses the same poloidal wavenumber k_y as CGYRO, but the normalizing magnetic field is $B_{\rm norm} = B_{\rm ref}$ [9] (the toroidal magnetic field at the magnetic axis). There can also be differences in the reference temperature and mass. In the gyrokinetc turbulence simulations of this paper it was assumed that for both codes: $T_{\rm norm} = T_e = T_i, m_{\rm norm} = m_i, Z_{\rm norm} = Z_i = 1.0$. Hence $\alpha_i = \sqrt{2}$. The two sources for the poloidal angular dependence of the wavevector are the magnetic field strength (B) and the gradient of the minor radius $|\nabla r|$ (equivalent to $|\nabla\psi| = RB_p$).

We seek to build a model, using the linear CGYRO eigenmode spectrum, for the normalized amplitude of the 3D potential fluctuations:

$$\Phi(k_y,k_x,\theta) = \frac{e|\tilde{\phi}|}{T_e\sqrt{dk_y dk_x}}\frac{a}{\rho_{B_{\rm norm}}}. \tag{8}$$

The factor $\sqrt{dk_y dk_x}$ in equation (8) is needed in order to make the intensity independent of the spacing between the wavenumbers dk_y and dk_x. For the zonal potential ($k_y = 0$) the dk_y is set to 1 in equation (8). The model for the peak of the potential amplitude is chosen to have the mode-coupling saturation form [5].

$$\Phi^{\rm model}_{k_y} = \frac{\gamma^{\rm eff}_{k_y}}{k_x^{\rm RMS}k_y}. \tag{9}$$

The primary goal of this paper is to determine the geometric factors required to generalize this model to be θ dependent. The model is exact if the effective growthrate $\gamma^{\rm eff}_{k_y}$ and the root mean squared (RMS) width of the radial wavenumber spectrum $k_x^{\rm RMS}$ are computed from the non-linear spectrum.

$$k_x^{\rm RMS} = \sqrt{\frac{\sum_{k_x} k_x^2\Phi^2(k_x,k_y,\theta)}{\sum_{k_x}\Phi^2(k_x,k_y,\theta)}}, \tag{10}$$

$$\gamma^{\rm eff}_{k_y} = k_x^{\rm RMS}k_y\Phi(k_x=0,k_y,\theta). \tag{11}$$

The model for the QL intensity is the flux surface average of the square of the peak amplitude:

$$I^{\rm model}_{k_y} = \left\langle\left(\Phi^{\rm model}_{k_y}\right)^2\right\rangle_\theta. \tag{12}$$

The factor $k_x^{\rm RMS}$ in equation (9) and the use of the the $k_x = 0$ peak in the definition for $\gamma^{\rm eff}_{k_y}$ (equation (11)) makes the model equation (9) independent of k_x. This model form has been found [5] to give a better fit to the way the fluxes fall off with k_y than other ways of modeling the impact of the k_x average of the flux calculation (equation (2)).

3. The role of the radial wavenumber spectrum width in turbulence saturation

In order to investigate the geometry dependence of the saturated potential intensity a set of gyrokinetic turbulence simulations were performed. A scan of the elongation of the flux surface (κ) changes the factor $B/B_{\rm unit}$ [4]. At the outboard midplane ($\theta = 0$) this factor scales like $1/\kappa$. The gradient of the minor radius at the outboard midplane is

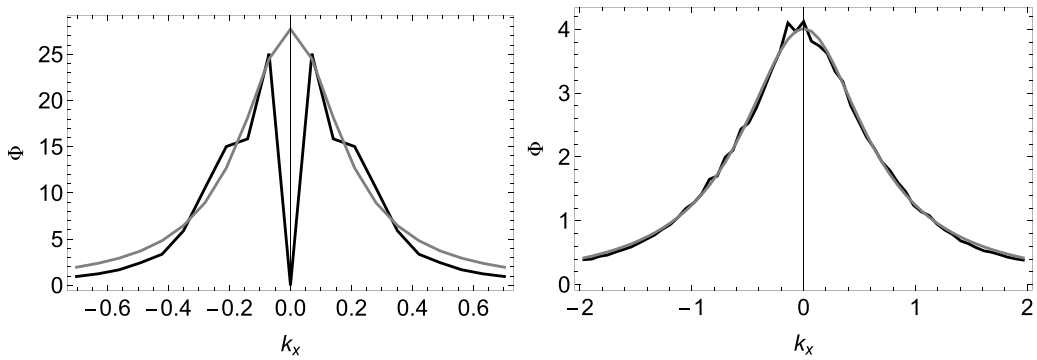

Figure 3. The normalized potential amplitude (equation (8)) k_x-spectrum (black) and Lorentzian fit (gray) for (left) the zonal $k_y = 0$ and (right) finite $k_y = 0.603$ fits at the outboard midplane for the GA-STD case.

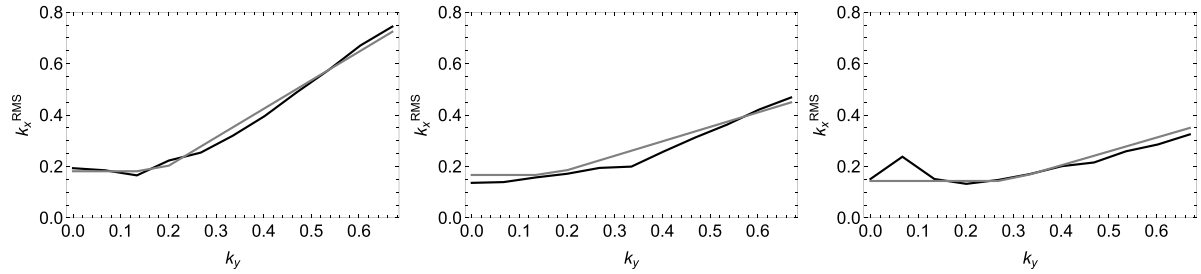

Figure 4. The kx-width computed from the potential intensity at the outboard midplane (black) and the model (gray) (equation (16)) for (left) GA-STD (center) $\kappa = 2.0$ and (right) $\Delta = -0.5$.

gradr0 $= |\nabla r|_{\theta=0} = 1/(1+\Delta)$ where $\Delta = dR_0/dr$ is the Shafranov shift of the major radius of the flux surface center (R_0). Starting with the GA-STD parameters ($a/L_n = 1$, $a/L_T = 3.0$, q = 2.0, $T_i/T_e = 1$, $\hat{s} = 1.0$, $\kappa = 1.0$, $\Delta = 0.0$, r/a = 0.5, R/a = 3.0), scans in $\kappa = (1.0, 1.25, 1.5, 1.75, 2.0)$ and $\Delta = (0.0, -0.1, -0.2, -0.4, -0.5)$ were run with CGYRO. A pure deuterium plasma, with a very low electron pressure (`BETAE_UNIT` = 0.0005), is assumed. For 7 of the cases the collision frequency of `NU_EE` $= \nu_{ee} a/c_s = 0.05$ was used. These cases had 24 positive poloidal wavenumbers with spacing $dk_y = 0.067$ and 144 positive radial wavenumbers with spacing $dk_x = 2\pi\hat{s}dk_y/N_{\rm box}$ where $N_{\rm box} = 6$ is the `BOX_SIZE` setting for CGYRO and $\hat{s} = 1$ is the magnetic shear. Another three cases were run with collision frequency `NU_EE` = 0.1 and $\Delta = 0$, -0.5, $\kappa = 2.0$ (16 $k_y's$ with $dk_y = 0.067$, 129 $k_x's$, $N_{\rm box} = 13$). These three cases were also run with GENE (20 $k_y's$ with $dk_y = 0.05$, 159 $k_x's$, $N_{\rm box} = 12$). One case was re-run with twice the value of dk_x in order to verify the scaling of the intensity with the radial wavenumber spacing. The 10 CGYRO cases were sufficient to deduce the dependence of the radial wavenumber width on the outboard midplane $|\nabla r|_0$ and $B(0)/B_{\rm unit}$ as discussed in this section. The GENE runs were used to verify the dependence on the reference magnetic field. The other normalizations were the same for both gyrokinetic codes.

The physical picture of the saturation of the gyrokinetic turbulence by zonal flow mixing [5] is that the $k_y = 0$ zonal fluctuations (non-static part) couple the fastest growing $k_x = 0$ modes at each k_y to slower growing, or damped, modes at larger k_x. This coupling is through non-linear advection by the time dependent zonal fluctuations (not zonal flow shear). It was shown in [5] that this mechanism was able to contribute to the saturation of even electron gyroradius scale modes, since the zonal flow mixing rate $\gamma_{ZF} = V_{ZF} k_y$ is able to compete with the linear growthrate γ_{k_y} at all k_y scales. The zonal ExB fluctuation saturates when the zonal flow mixing rate is balanced by the linear growthrate of the mode being advected. This gives an approximate relation for the RMS zonal ExB velocity that can be computed from the linear eigenmode spectrum:

$$V_{\rm ZF} = \max[\gamma_{k_y}/k_y]. \tag{13}$$

The growthrate is for the most unstable mode at each k_y. The RMS zonal flow velocity can be computed directly from the non-linear saturated spectrum:

$$V_{\rm ZF} = 0.5\sqrt{\sum_{k_x} k_x^2 \Phi^2(k_x, k_y = 0, \theta)}. \tag{14}$$

The first test of the geometry dependence is to check the zonal flow (ZF) mixing rule (equation (13)). The zonal flow velocity (equation (14)) at $\theta = 0$ and the right hand side of the ZF mixing rule (equation (13)) are plotted for the 10 cases in the κ and Δ scans in figure 2. The approximate ZF mixing rule equation (13) tracks the κ and Δ dependence pretty well. The factor of 0.5 is not optimal in equation (14) and becomes a fitting parameter in the saturation model. The important property is that the zonal flow mixing rule (equation (13)) captures the trend of the saturated zonal flow RMS velocity. The variation in the zonal velocity is much smaller than the factor

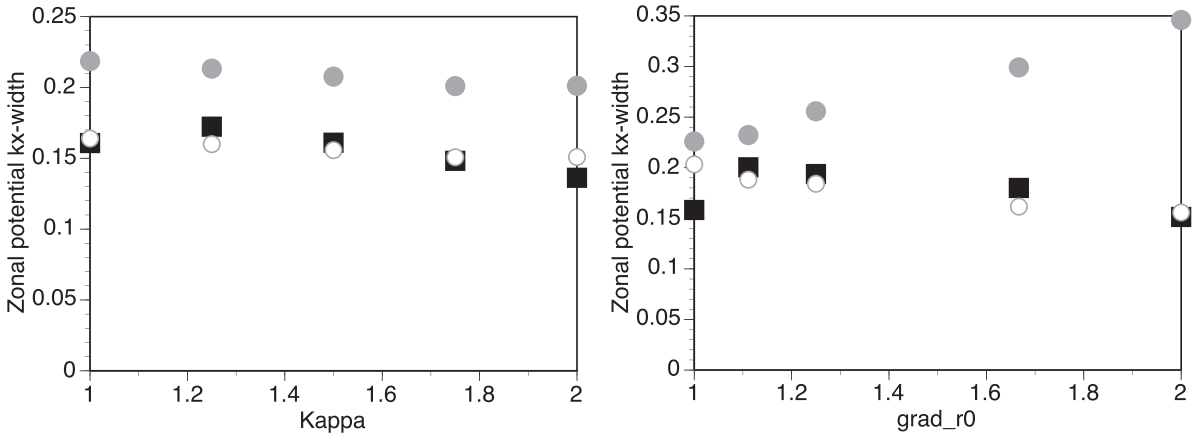

Figure 5. The zonal potential spectrum width $k_x^{\rm RMS}$ computed from the potential intensity at the outboard midplane (black, box) for (left) κ and (right) Δ scans also shown are the values of $k_{\rm ymax}$ (gray, circles) and $b_0 k_{\rm ymax}/|\nabla r|_0$ (open gray circles).

of two variation in $B(0)/B_{\rm unit}$ or $|\nabla r|_0$ and does not require any geometric correction. Note that the zonal flow velocity (equation (14)) is independent of the reference magnetic field since the gyroradius normalization of k_x and Φ cancel. The definition for V_{ZF} in equation (14) was changed from the original definition [5] to make this property obvious. It will be shown in the next section that the zonal potential is almost independent of the poloidal angle, so the ZF mixing rule holds approximately at all θ.

The RMS width of the k_x spectrum can be computed from equation (10) but this is not very accurate. The amplitude is well approximated by a Lorentzian function for moderate k_x/k_y but has a low amplitude tail at high k_x/k_y that makes using the formula equation (10) dependent on the range of k_x/k_y. To improve the calculation, a Lorentzian model was fit to the potential amplitude at the outboard midplane.

$$\Phi^{\rm fit} = \frac{\Phi_0}{(1+(\frac{k_x}{k_{x-{\rm width}}})^2)}. \tag{15}$$

The two parameters Φ_0 and $k_{x-{\rm width}}$ are determined by a least squares fit to a set of k_x points sampled from the potential. The shift in the peak of the potential due to equilibrium $E\times B$ velocity shear can be easily added to this model [10]. Evaluating $k_x^{\rm RMS}$ (equation (10)) with this Lorentzian model finds $k_x^{\rm RMS} = k_{x-{\rm width}}$. As shown in figure 3, the fit is very good for higher k_y but not as good for the zonal potential ($k_y = 0$). Note that the zonal potential at $k_x = 0$ is set to zero by the CGYRO code. The fit finder does not use this central point and it does not contribute to $V_{\rm ZF}$. The whole k_y spectrum of the $k_x^{\rm RMS}$ for the GA-STD case is shown in figure 4 (left). It has a pronounced flatness at low-k_y and is basically linear in k_y for higher values. A fit to this spectrum is shown in figure 4 given by the formula

$$\begin{aligned} k_x^{\rm model} &= \frac{B_{\rm unit}}{B_{\rm norm}} k_{\rm ycut}/|\nabla r|_0 \ \text{ for } \ k_y < k_{\rm ycut} \\ &= \frac{B_{\rm unit}}{B_{\rm norm}} \Big(k_{\rm ycut}/|\nabla r|_0 + b_1 (k_y - k_{\rm ycut}) G_q(0) \Big) \cdot \\ &\text{for } \ k_y \geq k_{\rm ycut} \end{aligned} \tag{16}$$

The cutoff is modeled by $k_{\rm ycut} = b_0 k_{\rm ymax}$ where $k_{\rm ymax}$ is the value of k_y where γ_{k_y}/k_y is maximum. The two fitting coefficients used in figure 4 are $b_0 = 0.83$, $b_1 = 1.31$. These were fit to the GA-STD case (left panel of figure 4). The geometric coefficients in equation (16) were determined by the κ and Δ scans. The two ends of these scans $\kappa = 2.0$ (center panel) and $\Delta = 0.5$ (right panel) are shown in figure 4. The change in slope and the nearly constant value of the width at $k_y = 0$ are well fit by this model with the same coefficients. The oscillations at low-k_y suggest that there are slowly evolving contributions to the potential spectrum that have not been time averaged sufficiently. The GENE simulations are well fit by the same model (equation (16)) verifying the overall $B_{\rm norm}$ factor.

The width of the zonal potential fluctuation amplitude tracks with $b_0 k_{\rm ymax}/|\nabla r|_0$ as shown in figure 5. The best fit between the width of the zonal potential spectrum and $b_0 k_{\rm ymax}/|\nabla r|_0$ is $b_0 = 0.75$ for the κ scan and $b_0 = 0.9$ for the Δ scan. There is a lot of variation in the quality of the Lorentzian fit to the zonal potential so these differences are probably not significant. The best fit to the GA-STD case of $b_0 = 0.83$ used in figure 4 is within this range.

This model for $k_x^{\rm RMS}$ (equation (16)) is an improvement at low-k_y over the original model (SAT1) in reference [5] that had $k_x^{\rm model} = k_y$ in the ion range of $k_y < 1$. If the denominator of the model for the potential (equation (9)) was chosen to be $K_{i\perp}^2$ instead of $k_x^{\rm RMS} k_y$, the width of the k_x spectrum at $\theta = 0$ would be $k_x^{\rm model} = k_y G_q(0)/|\nabla r|_0$. This is similar to equation (16) for $k_y > k_{\rm ycut}$ except for the extra factor of $|\nabla r|_0$. The Δ scan in figure 4 rules this factor out. Using $K_{i\perp}^2$ in the model for the potential would also not reproduce the observed flattening of $k_x^{\rm RMS}$ at low k_y.

The effective non-linear growthrate $\gamma^{\rm eff}$ can be computed from the non-linear potential spectrum using the $k_x^{\rm RMS}$ determined by the spectrum in equation (11). As has been observed for many spectra, the effective growthrate is quite flat and independent of k_y above $k_{\rm ymax}$, where the maximum in γ_{k_y}/k_y occurs, as shown in figure 6. The non-linear effective growthrate is well fit by the linear growthrate γ_{k_y} for $k_y < k_{\rm ymax}$. For the GA-STD case, the effective growthrate is well modeled by

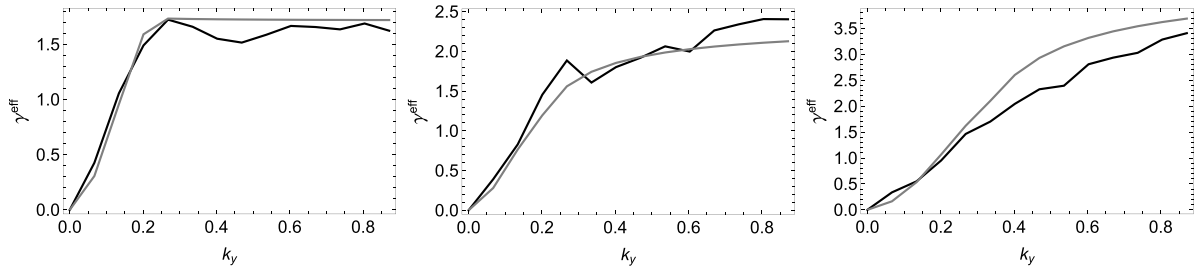

Figure 6. The $\gamma^{\rm eff}_{k_y}$ spectrum computed from the potential at the outboard midplane (black) equation (11) and $G(0)\gamma^{\rm model}_{k_y}$ (gray) for the GA-STD case (left) the case $\kappa = 2.0$ (middle) and the case $\Delta = -0.5$ (right).

$$\gamma^{\rm model}_{k_y} = b_2\gamma_{k_y} \text{ for } k_y < k_{y\max} \\ = b_2\gamma_{\max} \text{ for } k_y \geq k_{y\max}. \tag{17}$$

Here $\gamma_{\max}$ is the value of the linear growthrate at $k_{y\max}$. The best fit for the outboard midplane is $b_2 = 7.5$. This model (equation (17)) is simpler than the original SAT1 model [5] since it does not have the subtraction of the zonal flow mixing term that was included in the original model for $k_y \leq k_{y\max}$. The new model (equation (17)) is a better fit to $\gamma^{\rm eff}_{k_y}$ (figure 6 (left)) in this range of k_y .

The slope of $\gamma^{\rm eff}$ with k_y changes with both κ and Δ away from the GA-STD case. Using information from the next section on the poloidal dependence of the spectrum, a form factor $G(0)$ is proposed here to modify the model for $\gamma^{\rm eff}$ at the outboard midplane.

$$G(0) = 1.0 \text{ for } k_y < k_{y\rm cut} \\ = \sqrt{(k_{y\rm cut} + b_3(k_y - k_{y\rm cut})/G_q^2(0))/k_y} \text{ for } k_y \geq k_{y\rm cut}. \tag{18}$$

The $\gamma^{\rm eff}_{k_y}$ computed from the potential spectrum (black) and the model $G(0)\gamma^{\rm model}_{k_y}$ (grey) are shown in figure 6 for $b_3 = 0.7$. The left panel of figure 6 is the GASTD case. Without G(0) all of the cases would be flat for $k_y > k_{y\max}$. The geometric factor G(0) changes the slope of the model with k_y. This change in slope is most clear in the highest range of $\kappa = 2.0$ (center panel) and $\Delta = -0.5$ (right panel) of figure 6. These two cases were run with a different collision frequency than the others and a smaller range of k_y and k_x. The GENE runs of these same cases show the same increase in slope. The need for the geometry factor $G(0)$ is better motivated by the poloidal dependence of the intensity as will be discussed in the next section.

4. Poloidal angular dependence of the 3D potential fluctuation intensity

In order to make a clear distinction in the poloidal angle dependence between the two geometric factors (B and $|\nabla r|$), CGYRO runs were done at $\kappa = 1.5$ and $\Delta = -0.25$ and RMIN $= 0.8$, NU_EE $= 0.05$ with the same poloidal and radial wavenumber resolutions as the 7 other CGYRO runs at this collision frequency. These choices make the magnetic field a broad function of θ and the factor $|\nabla r|$ a narrow function of θ that changes slope at $\theta = \pi$. Two cases with different magnetic shear $\hat{s} = 1.0, 0.5$ were run. The 2D intensity of potential fluctuations was saved at eight points: $\theta = -\pi, -3\pi/4 - \pi/2, -\pi/4, 0, \pi/4, \pi/2, 3\pi/4$. Where θ is the Miller geometry angle [7]. The ratio $\theta_x = k_x/(\hat{s}k_y)$ is a useful coordinate for plotting since it is involved in the ballooning space extension of θ. The θ_x-spectrum of the normalized potential amplitude Φ for $k_y = 0.25, \hat{s} = 1.0$ is plotted for the negative θ values in figure 7 (left). The positive θ spectra are essentially the mirror image of the negative ones about the $k_x = 0$ axis. From figure 7 it is clear that there is a peak at $k_x = 0$ and there is a skew towards the $+\theta$ direction. The case $\theta = -\pi$ on the right panel of figure 7 shows that there is an approximate reflection symmetry about the line $\theta_x = \pi$ with a second peak at $\theta_x = 2\pi$ with the same amplitude as the peak at $\theta_x = 0$. The value at $\theta_x = \pi$ is lower than the two peaks for $k_y < k_{y\max}$ and is the dominant peak for $k_y > k_{y\max}$ for $\theta = -\pi$. The symmetry of the spectrum at $\theta = -\pi$ can be understood from the quasi-periodicity of the eikonal [3].

$$\tilde{\phi}(k_y, k_x, \theta) = \tilde{\phi}(k_y, k_x - 2\pi\hat{s}k_y, \theta + 2\pi). \tag{19}$$

Due to this quasi-periodicity property, the peak of the potential at $\theta = -\pi$ and $\theta_x = 2\pi$ in the right panel of figure 7 is the image of a peak at $\theta_x = 0$, $\theta = \pi$. The spectrum at $\theta = \pi$ is the reflection of the plot in figure 7 (right) about the line $\theta_x = 0$. There are no peaks at larger values of $|\theta_x| > 2\pi$ so really there is only the peak at $\theta_x = 0$ and its images at $\theta_x = \pm 2\pi$ within the range of θ.

The 3D spectrum in the space k_y, k_x, θ is like a house of mirrors with internal reflections due to the dual nature of k_x both as a Fourier wavenumber for the radial coordinate and as the enforcer of the quasi-periodicity property. The potential spectrum can be mapped onto an extended ballooning angle coordinate θ_b. This coordinate extends the range of $-\pi \leq \theta \leq \pi$ by adding a translation in θ_x by 2π at the boundary of each circuit of θ This continues for each θ circuit until the limit of the range of θ_x is reached. The independent ballooning modes can be labeled by $k_{x0} = \ell dk_x = \ell\hat{s}dk_y 2\pi/N_{\rm box}$ with the integer ℓ having the range $-(N_{\rm box} - 1) \leq \ell \leq (N_{\rm box} - 1)$. For the case $\hat{s} = 1.0$ there are 11 k_{x0}'s ($N_{\rm box} = 6$). The quasi-periodicity property equation (19) can be used to map the potential onto the ballooning mode space for each independent ballooning mode. The result is shown in figure 8 for $k_y = 0.25, \hat{s} = 1$. The highest peak is for $\ell = 0$, the next highest pair $\ell = \pm 1$ etc down to the lowest amplitude pair $\ell = \pm 5$. Most

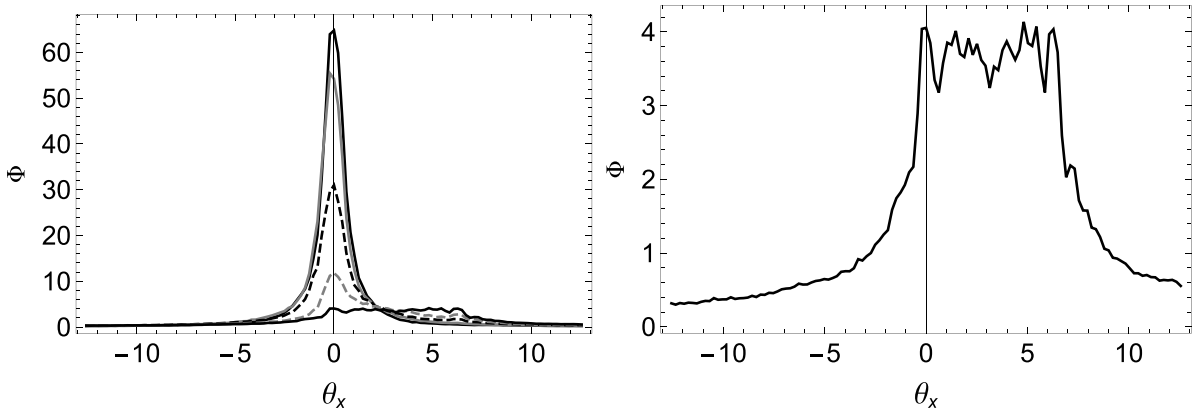

Figure 7. The $\theta_x = k_x/(\hat{s}k_y)$ spectrum of the normalized potential amplitude Φ for $k_y = 0.25$ and $\hat{s} = 1.0$ for (left) $\theta = 0$ (highest solid black), $-\pi/4$ (solid gray), $-\pi/2$ (dashed black), $-3\pi/4$ (dashed gray), $-\pi$ (lowest solid black) and (right) just $\theta = -\pi$.

of the amplitude of all of the ballooning modes is within the original range ($\pm\pi$) of θ. The width of all of the ballooning modes is mostly contained in the envelope of the $\ell = 0$ mode.

The θ dependence of the potential at $k_x = 0$ is the same in the original theta space and in ballooning space within the first panel. The theta dependence of the intensity at $k_x = 0$ for all of the k_y's is shown in figure 9. The intensity has been normalized to the intensity at $\theta = 0$. The left panel shows the range $0 \le k_y \le 0.55$. For this case $k_{y\max} = 0.246$ so it is within this range. The zonal intensity $k_y = 0$ (highest curve in left panel) is the peak of the fitted Lorentzian shown in figure 3. It is almost independent of θ. This is representative of the whole zonal k_x-spectrum that is remarkably independent of poloidal angle. The shape becomes progressively narrower (left panel) for increasing k_y until it saturates. The right plot in figure 9 has all of the other values $0.6 \le k_y \le 1.15$. The shape of the intensity is the same for all these values. It is not hard to imagine that this result could be due to the non-linear convolution of the zonal potential with the finite k_y potential causing a broadening of the θ dependence at low k_y along with the broadening of the $k_x^{\rm RMS}$ width. However, the shapes for $k_y = 0.05, 0.1, 0.15$ are nearly the same rather than broadening towards $k_y = 0$.

Two geometric shape functions have been found that fit the two ends of the k_y spectrum.

$$G_1 = \left(\frac{B(0)}{B(\theta)}\right)^4 \tag{20}$$

$$G_2 = \left(\frac{B(0)}{B(\theta)}\right)^4 \left(\frac{|\nabla r|}{|\nabla r|_0}\right)^4 = \left(\frac{G_q(0)}{G_q(\theta)}\right)^4. \tag{21}$$

These two shape functions are shown in figure 10. The magnetic field shape function (G_1) (gray) is broader and fits the low $k_y = 0.1$ intensity shape (black) very well as shown in the left plot. The shape function G_2 has the factor G_q that appears in the model for the $k_x^{\rm RMS}$ (equation (16)) but raised to the fourth power. These shape factors are normalized to the outboard miplane value like the intensities in figure 10. The second shape factor (gray dashed) is a very good fit to the higher k_y spectrum (black) shown in the right panel of figure 10. These two shape functions will be used in the next

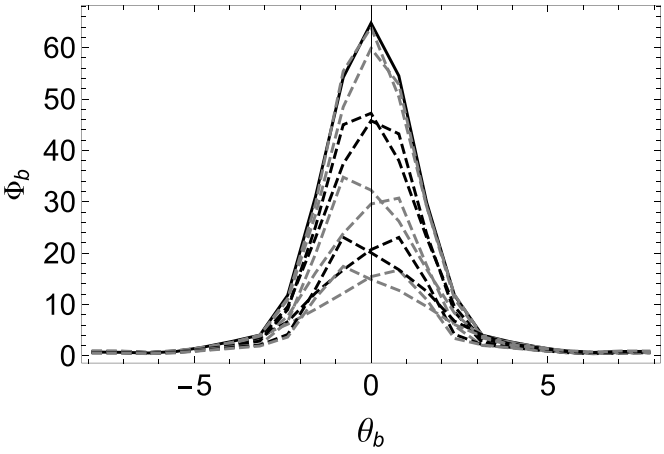

Figure 8. The ballooning angle θ_b dependence of the amplitude of the potential Φ_b for the 11 independent ballooning modes of the CGYRO spectrum for $k_y = 0.25$.

section to build a model that interpolates between them to cover all k_y. A CGYRO simulation was run for the same case but with magnetic shear of $\hat{s} = 0.5$. This was run to see if the shape changes with magnetic shear. The two shape functions G_1 and G_2 do not depend upon shear but the perpendicular wave vector $K_{i\perp}^2$ evaluated at $k_x = 0$ does. It was found that the shape at $\hat{s} = 0.5$, at low and high k_y, was the same as for $\hat{s} = 1.0$. The perpendicular wave vector would give a shape function that was independent of k_y and broader for $\hat{s} = 0.5$, so it cannot reproduce the observed non-linear intensity spectrum. Once again, this rules out the use of $K_{i\perp}^2$ as the denominator of the model of the potential spectrum.

Similarly, the lack of magnetic shear dependence also rules out the following extension of the Lorentzian model to fit the $\theta = 0$ spectrum:

$$1/\left(1 + \left(\frac{\hat{s}k_y\theta}{k_x^{\rm RMS}}\right)^2\right)^2. \tag{22}$$

This shape function comes from assuming that k_x in equation (15) is replaced by $k_x + \hat{s}k_y\theta$ in general and then taking $k_x = 0$ to get equation (22). The difference between θ and

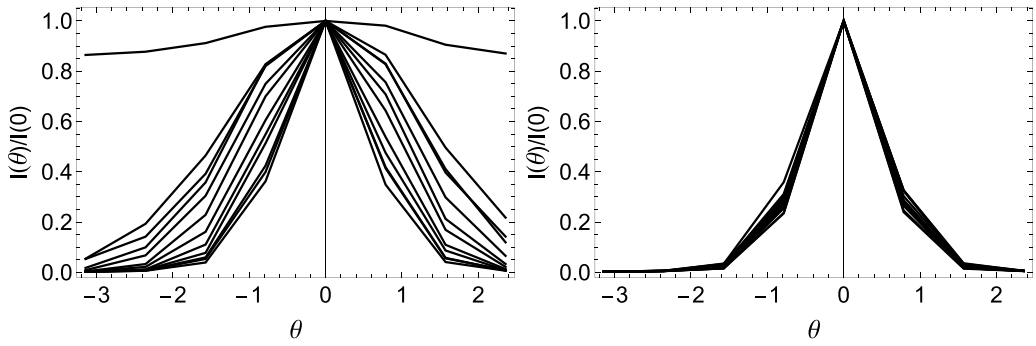

Figure 9. The intensity for $k_x = 0$ normalized to $\theta = 0$ for (left) $0 \le k_y \le 0.55$ and (right) $0.6 \le k_y \le 1.15$.

Θ in equation (4) is not important for this argument. The problem with the shape function equation (22) is that the $k_x^{\rm RMS}$ computed by fitting the spectrum at $\theta = 0$ does not depend on magnetic shear $\hat{s}$ and neither does the shape in θ of the non-linear potential spectrum figure 9.

The shape function G_1 could be replaced by the Gaussian envelope of the linear eigenmodes. This is appealing, and can give a good fit to the low k_y spectrum. However, as we will see in the next section, when you include the peak amplitude of the potential in the fit to the QL intensity, the θ dependence of G_1 is un-modified but G_2 is replaced by $(G_q(\theta)^{-4}$ for the best fit. Hence, G_1 is not a common factor of these two shape functions in the final analysis and it cannot be replaced by a Gaussian envelope in both shape functions as would be the case if it were from the wavefunction envelope.

Note that the flux surface average of the fluxes employed in the gyrokinetic codes covers only the range of θ. It is the sum over k_x that includes the extended ballooning angle. The potential intensity is very small for $|\theta_x| \ge 2\pi$ so the ballooning mode extensions do not contribute much to the flux. The simplest interpretation, that the shape in θ of the potential intensity spectrum at $k_x = 0$ comes from the geometric factors in equations (20) and (21), holds up to this analysis of alternatives. It does not prove it is unique and should be tested on more cases.

5. A model of the intensity required for a quasi-linear flux calculation

Until now, the 3D intensity of potential fluctuations has been examined in various ways to reveal the shape dependence. Now the ultimate goal of modeling the QL intensity required to compute the fluxes will be addressed. The QL intensity involves a flux surface average and a sum over k_x of the intensity weighted by the QL weight (cross-phases) of all of the modes in the non-linear spectrum. Only the QL weight of the most unstable mode was used to compute the QL intensity (equation (1)). Each of the independent ballooning modes with different values of k_{x0} contribute to the flux in some way. Therefore, it is expected that the QL intensity is not just the flux surface average of the 3D intensity evaluated at $k_x = 0$ or summed over k_x without the QL weights of the non-zero k_{x0} ballooning modes. This is easily shown by comparing the QL weight computed from the spectrum with these two proxy candidates. This is a distraction from the goal of building a model of the QL intensity directly from the linear CGYRO eigenvalue spectrum so it will not be presented here. Models for $k_x^{\rm model}$ (equation (16) and $\gamma_{k_y}^{\rm model}$ (equation (17)) have already been found and can provide a useful template for the final construction. The model template is:

$$Q_{ak_y}^{\rm model} = \frac{\alpha_i dky}{|\nabla r|_0} I_{k_y}^{\rm model} W_{ak_y}^{QL}. \tag{23}$$

Here the poloidal wavenumber interval has been chosen to be $\Delta_{k_y} = dK_{iy}$ computed from equation (5). This interval is needed because the ion Bessel function makes the intensity and quasi-linear weight a function of the ion poloidal wavenumber K_{iy} so the integral of the flux per mode should have the measure dK_{iy}. As shown in figure 5 *kymax* tracks with the outboard midplane value of $|\nabla r|_0$ so this is used in the measure in equation (24).

The model for the quasi-linear intensity is taken to have the form:

$$I_{k_y}^{\rm model} = \left\langle G^2(\theta) \right\rangle_\theta \left(\frac{\gamma_{k_y}^{\rm model}}{k_x^{\rm model} k_y} \right)^2. \tag{24}$$

For simplicity, all of the θ dependence is absorbed into $G(\theta)$

$$\begin{aligned} G^2(\theta) &= d_1 G_1(\theta) \text{ for } k_y < k_{\rm ycut} \\ &= \left(d_1 G_1(\theta) k_{\rm ycut} + b_3 d_2 G_2(\theta)(k_y - k_{\rm ycut}) \right)/k_y \text{ for } k_y \ge k_{\rm ycut} \end{aligned} \tag{25}$$

where the best fit for the coefficients d_1, d_2 is found to be

$$d_1 = \left(\frac{B_{T_0}}{B(0)} \right)^4 \tag{26}$$

$$d_2 = 1/G_q(0)^2. \tag{27}$$

The model $k_x^{\rm model}$ was fit to the outboard midplane $k_x^{\rm RMS}$. This leaves it ambiguous if the geometric factors become functions of θ in general. The best fit coefficient d_1 (equation (26)) cancels the dependence of G_1 on minor radius r contained in $B(0)$ by replacing it with the toroidal magnetic field at the flux surface center $B(0)|_{r=0} = B_{T_0}$. This was required in order for the

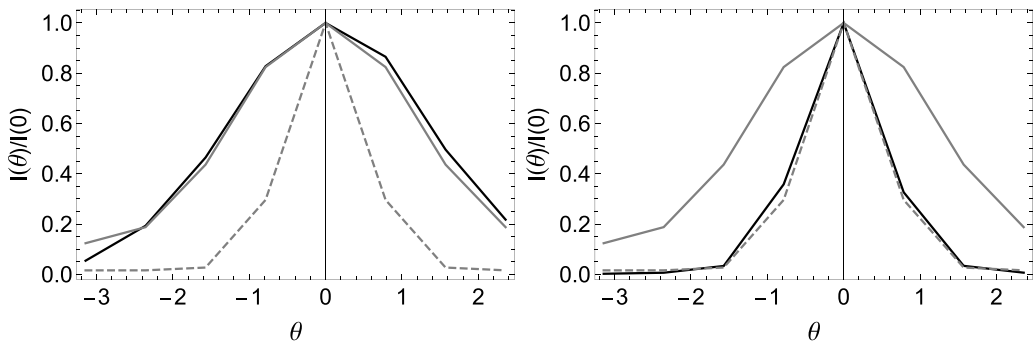

Figure 10. The intensity for $k_x = 0$ normalized to $\theta = 0$ (black) for $k_y = 0.1$ (left) and $k_y = 0.65$ (right) and two shape functions G_1 (grey) and G_2 (gray dashed).

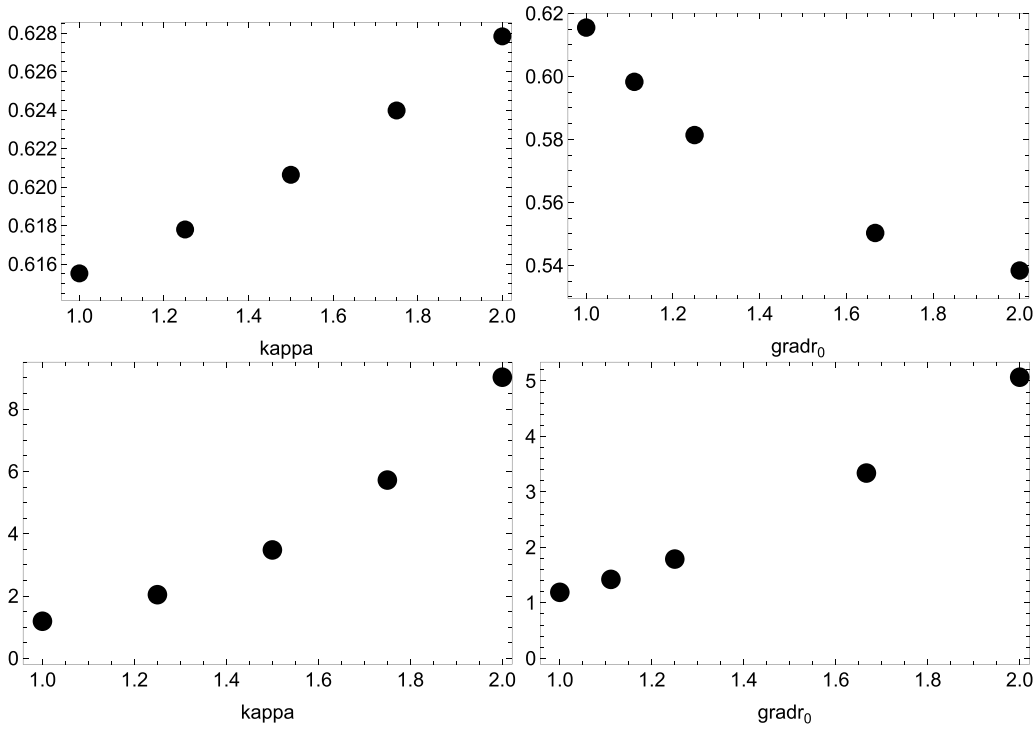

Figure 11. The flux surface averages $\hat{G}_1$ (top) and $\hat{G}_2$ (bottom) for the κ (left) and gradr0 $= 1/(1+\Delta)$ (right) scans.

model to fit the two cases that were run at larger $r/a = 0.8$ to explore the poloidal angular dependence of the intensity. This has been verified with a scan in r/a that will be reported in a separate paper on a large CGYRO database verification of the model to follow. It is important for G^2 to have the same $k_{\rm ycut}$ as $k_x^{\rm model}$. For $k_y \geq k_{\rm ycut}$, the factor $G_q(0))$ in $k_x^{\rm model}$ does get promoted to its θ dependent form. This contributes two powers to G_2. The other two powers are needed to fit $\gamma_{k_y}^{\rm eff}$ (equation (18)). The best fit for the coefficient d_2 (equation (27)), changes $d_2 G_2/(k_x^{\rm model} k_y)^2$ to the shape factor $(G_q(\theta)k_y)^{-4}$ for $k_y >> k_{\rm ymax}$. Since $G^2(\theta)$ is linear in G_1 and G_2 the flux surface average of these terms can be computed separately and then used in the formula for the intensity model equation (24).

To see how these weight the model for the QL intensity, the flux surface averages $\hat{G}_1 = \left\langle G_1 \right\rangle_\theta$ and $\hat{G}_2 = \left\langle G_q^{-4} \right\rangle_\theta$ are plotted in figure 11 for the κ and Δ scans. The flux surface average $\hat{G}_1$ (top plots) is weakly varying. It has an influence on the slope of the very low $k_y < k_{\rm ymax}$ part of the spectrum and the peak value of the QL intensity model plotted in figure 12. The flux surface average $\hat{G}_2$ (bottom plots of figure 11) has a strong variation with both κ and Δ (gradr0). This is primarily due to the variation of $G_q^{-4}(0)$. The $\hat{G}_2$ factor impacts the way the intensity falls off with k_y for $k_y >> k_{\rm ymax}$. The effect can be clearly seen in figure 12. The QL intensity spectrum, computed from the CGYRO Q_e, (black) is much broader for the $\kappa = 2.0$ (center) and gradr0 $= 2.0$ (i.e. $\Delta = -0.5$) (right) than the GASTD case (left). All of these cases are with the same collision frequency (0.1). The broadening for the Δ scan is partly due to the higher k_y of the peak due to $k_{\rm ymax}$ as seen in figure 5. The value of the geometry factor $\hat{G}_2$ is largest for $\kappa = 2.0$ and its effect on the spectrum is important for the accuracy of the fluxes and the overall scaling of the fluxes with κ and gradr0.

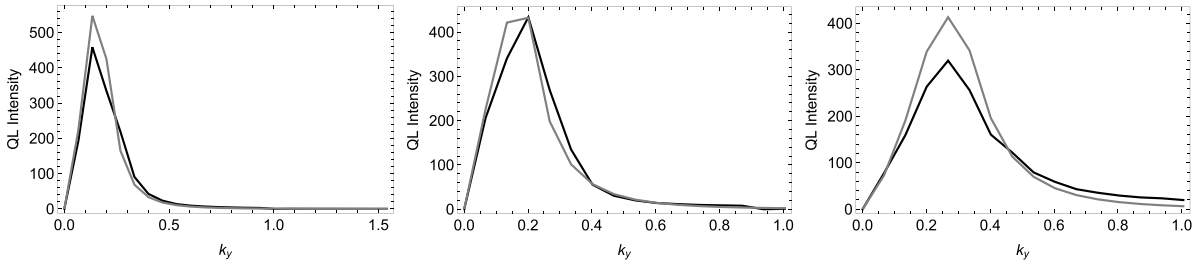

Figure 12. The QL intensity (black) and the optimum fit model (gray) equation (24) for GASTD (left), $\kappa = 2.0$ (middle) and $\Delta = -0.5$ (right) all with collision frequency 0.1.

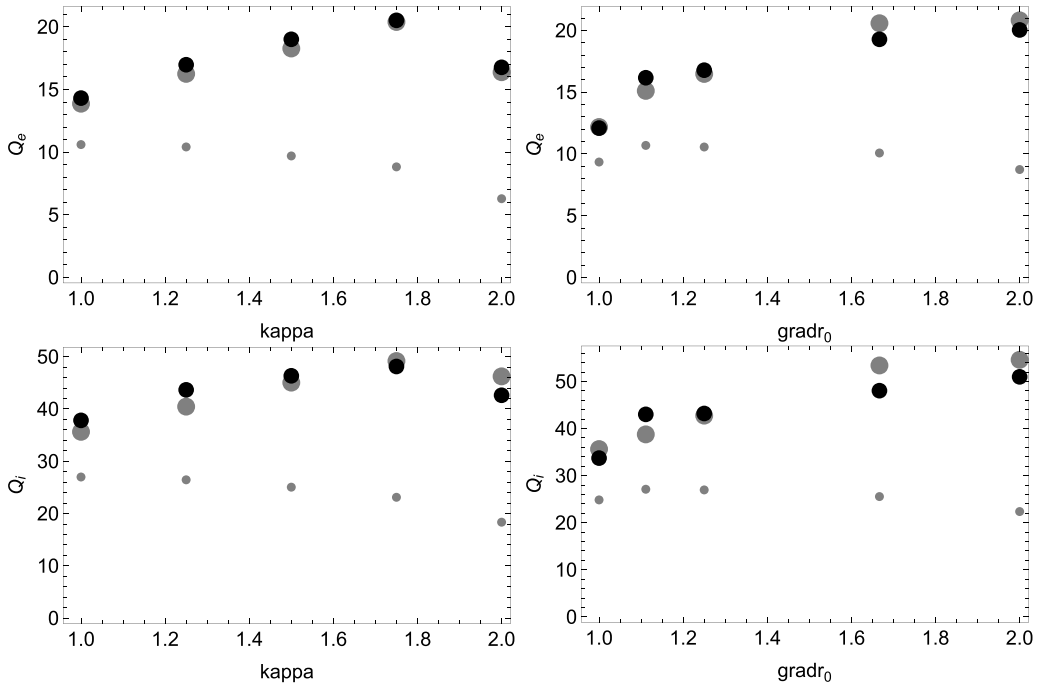

Figure 13. The total electron (top) and ion (bottom) energy fluxes for a κ scan (left) and a gradr0 $= 1/(1+\Delta)$ scan (right) for CGYRO (black), optimum model (large gray) and the original SAT1 model (small gray).

There are four fitting coefficients in the model template (equation (24)) b_0, b_1, b_2, b_3. The coefficient b_2 from $\gamma_{k_y}^{\text{model}}$ (equation (17)) acts as an overall multiplier. It will be determined by setting the net offset of the model fluxes and the CGYRO fluxes for the ten cases (scans in κ and Δ) to zero. The other three coefficients will be adjusted to find the minimum RMS error between the model and CGYRO for the per k_y flux contributions. There are 10 CGYRO runs and 14 k_y's included in the RMS error for both electron and ion fluxes for a total of 280 data points being fit. The optimum coefficients were found to be $b_0 = 0.72$ for k_{ycut}, $b_1 = 1.22$ for the slope of k_x^{model}, $b_3 = 2.40$ for the slope of G^2 and $b_2 = 2.82$ for the zero offset condition. Note that b_2 was decreased and b_3 was increased because $d_1 = 1.826$ for the GASTD case rather than 1.0. These values give an RMS error average of 0.52 GB units for each k_y flux contribution. The error for the total fluxes for the whole set of 10 cases are 4.1% for Q_e and 6.9% for Q_i. The total fluxes for each scan are shown in figure 13. The overall trend of the fluxes with κ and gradr0 is very well matched. Recall that the $\kappa = 2.0$, gradr0 $= 1.0$, 2.0 CGYRO runs were done with a higher collision frequency (0.1) than the others (0.05) which lowers the fluxes for these points. The overall scaling trend is approximately $Q \propto 1/G_q(0)$. This optimum fit is a fairly broad minimum of the coefficients.

The result of computing the SAT1 model fluxes [5] using the CGYRO linear eigenmode spectrum is also shown in figure 13 as small gray dots. The trend of the fluxes is flat or downward for both scans. The SAT1 model does not have any explicit geometric terms. It is effectively assuming that B_{unit} is the natural magnetic field that sets the local turbulence gyroradius and eddy size. This model was calibrated to a set of 83 GYRO [11] simulations that included κ scans but not Δ scans. The simulation database was assembled 15 years ago in order to calibrate the original (SAT0) TGLF transport model [12]. Low poloidal and radial grid resolutions were used in order to speed up the simulations. GYRO uses a grid in the minor radius so that it can run both periodic and non-periodic (global) gyrokinetic simulations. It can compute gyro-averages with spectral accuracy (like CGYRO) using an exact Bessel function expansion, but this is expensive and was not done for these runs. The trend with κ for these low-resolution GYRO runs agrees with the SAT1 model fluxes in figure 13. This is a lesson

learned. A model is no more accurate than the simulations it fits. It also is a caution to present day attempts to run reduced physics fidelity global simulations in order to capture long range wave-like effects. The reduced simulation models may not capture important local physics effects, like the geometric effects in this paper, that require accurate gyro-averaging (i.e. Bessel functions).

6. Summary

This paper presented the most accurate model of the flux spectrum ever developed for quasi-linear modeling. It is as accurate as the agreement between different gyrokinetic codes. It will not be as accurate on a larger set of gyrokinetic runs as it is for the 10 runs it was calibrated to. It will be shown in a separate paper that the fitting coefficients for the poloidal wavenumber (k_y) dependent geometry factor (equation (25)) and the models for the radial wavenumber spectral width (equation (16)), and the effective growth rate (equation (17)) (other than the overall norm) presented in this paper do not need to be changed in order to give a good fit to a much wider ranging database. The spectral shift model for $E \times B$ shear [10] and the electron scale turbulence [5] will also be re-calibrated in the separate paper.

Previous experience with quasi-linear models leads to the expectation that the new model will have sufficient accuracy for modeling the core transport of tokamaks under normal conditions. The improvements in the flux surface shape fidelity of SAT2 will be validated for near edge L-mode conditions where an under-prediction of the transport has been found with TGLF [13]. A similar under-prediction of transport by TGLF during the current ramp-up phase has also been reported [14] and will be revisited with this new model. The recent experimental observation of improved energy confinement with negative triangularity [15] will also make a good validation test of the shape factors in the new model. High bootstrap fraction tokamak discharges, with a strong Shafranov shift reducing transport in the core, have been difficult to predict [16]. Perhaps the SAT2 model will improve the plasma profile predictions. This regime looks to be very attractive for steady state tokamak reactors experimentally [17] with enhanced energy confinement. The prediction of transport in low aspect ratio spherical tori, which have strongly varying shape factors and a large Shafranov shift, will also be used to validated the SAT2 model.

This paper lays out new methodologies, like fitting to the QL intensity and 3D potential intensity. By computing the linear spectrum, and quasi-linear weights, with the same gyrokinetic code as the simulations, the process of modeling the QL intensity can be separated from the process of developing a fast reduced linear eigensolver by this approach.

The role of zonal flow mixing on setting the width of the k_x-spectrum for the finite k_y modes was explored in this paper. It was shown for the first time that the width of the zonal potential spectrum provides an irreducible minimum width. It was also shown that this width is coupled to the value of $k_{y\max}$ that also plays a role in setting the saturated RMS velocity of the zonal fluctuations through balancing the zonal flow mixing rate with the linear growthrate $\gamma_{\max}$ (equation (13)). This saturation rule for the zonal flow velocity was found to be independent of geometry. The width of the k_x-spectrum has a dependence on geometry (equation (16)). For large k_x, this is consistent with the Bessel functions depending on K_{ix} (equation (6)). The argument of the Bessel function has the physical total magnetic field gyro-radius normalizing the radial wavenumber. Hence, the radial correlation length at the outboard midplane scales with the local total magnetic field. At low k_x the influence of the zonal flow mixing takes over and the poloidal wavenumber argument of the Bessel function (equation (5)) sets the geometry dependence. The form of equation (5) shows that the toroidal correlation length scales with the poloidal magnetic field gyroradius. The new model for k_x^{RMS} (equation (16)) is an improvement over the SAT1 model.

The model for the effective non-linear growthrate $\gamma_{k_y}^{\mathrm{eff}}$ at low-k_y was also improved in this paper (equation (17)). It was found that there was no need for the zonal flow mixing subtraction used in the SAT1 model below the peak at $k_{y\max}$. This is because the flattening of k_x^{RMS} at low k_y, due to the zonal potential setting a minimum width, suppresses the transport at low k_y enough. No additional suppression is required in the model. This change to the model improves the fit to the QL intensity at low k_y significantly. An overall geometric factor was found to be needed in order to match the change in slope of $\gamma_{k_y}^{\mathrm{eff}}$ at high k_y with flux surface shape. This shape factor is consistent with the findings of the poloidal dependence of the peak intensity at $k_x = 0$.

Perhaps the most controversial part of the analysis of the 3D spectrum in this paper is the finding that the poloidal dependence of the peak of the intensity spectrum at $k_x = 0$ can be fit with purely geometric factors. This conclusion is based on only two cases ($\hat{s} = 1.0, 0.05$) so it will need further verification. Clearly, the geometric factors fit the spectra in figure 10 for the cases tested, but it was expected that some dependence on the shape of the most unstable linear eigenmode wavefunction would be found. It is interesting that the linear eigenmodes found with TGLF have a Gaussian envelope that is not far from the shape of $(B(0)/B)^2$ at low-k_y. The wavefunction envelope becomes narrower at higher k_y. It may be that this is caused by the same geometric factors entering the linear TGLF equations (velocity moments of the gyrokinetic equations). The non-linear turbulence spectrum includes all modes, not just the most unstable one, so the wavefunction shape may become washed out in the non-linear simulation but the quasi-linear weight, that depends on the eigenmode frequency, is still preserved by the turbulence. Further study is required to follow up on these questions.

Acknowledgments

Discussions with J Citrin, P Mantica R Waltz and H Dudding contributed to this work. This work was supported by the U.S. Department of Energy under DE-SC0019736, DE-SC0018990, DE-FG02-95ER54309, and DE-FC02-04ER54698. This work has been carried out within the framework of the EUROfusion Consortium and has received funding from the Euratom research and training programme

2014–2018 and 2019–2020 under grant agreement No 633053. This work was supported by the Engineering and Physical Sciences Research Council [EP/L01663X/1]. We acknowledge the CINECA award under the ISCRA initiative, for the availability of high performance computing resources and support. Computing resources were provided by the Oak Ridge Leadership Computing Facility under Contract DE-AC05-00OR22725 and the National Energy Research Scientific Computing Center under Contract DE-AC02-05CH11231.

Disclaimer

The views and opinions expressed herein do not necessarily reflect those of the European Commission. This report was prepared as an account of work sponsored by an agency of the United States Government. Neither the United States Government nor any agency thereof, nor any of their employees, makes any warranty, express or implied, or assumes any legal liability or responsibility for the accuracy, completeness, or usefulness of any information, apparatus, product, or process disclosed, or represents that its use would not infringe privately owned rights. Reference herein to any specific commercial product, process, or service by trade name, trademark, manufacturer, or otherwise, does not necessarily constitute or imply its endorsement, recommendation, or favoring by the United States Government or any agency thereof. The views and opinions of authors expressed herein do not necessarily state or reflect those of the United States Government or any agency thereof.

ORCID iDs

G M Staebler https://orcid.org/0000-0002-1944-1733
J Candy https://orcid.org/0000-0003-3884-6485
B Patel https://orcid.org/0000-0003-0121-1187

References

[1] Waltz R E, Staebler G M, Dorland W, Hammett G W, Kotschenreuther M and Konings J A 1997 A gyro-landau fluid transport model *Phys. Plasmas* **4** 2482
[2] Staebler G M, Kinsey J E and Waltz R E 2005 Gyro-landau fluid equations for trapped and passing particles *Phys. Plasmas* **12** 102508
[3] Candy J, Belli E A and Bravenec R V 2016 A high-accuracy eulerian gyrokinetic solver for collisional plasmas *J. Comput. Phys.* **324** 73–93
[4] Waltz R E and Miller R L 1999 Ion temperature gradient turbulence simulations and plasma flux surface shape *Phys. Plasmas* **6** 4265
[5] Staebler G M, Candy J, Howard N T and Holland C 2016 The role of zonal flows in the saturation of multi-scale gyrokinetic turbulence *Phys. Plasmas* **23** 062518
[6] Howard N T, White A E, Greenwald M, Holland C and Candy J 2014 Multi-scale gyrokinetic simulation of Alcator C-Mod tokamak discharges *Phys. Plasmas* **21** 032308, 201
[7] Miller R L, Chu M S, Greene J M, Lin-liu Y R and Waltz R E 1998 Non-circular, finite aspect ratio, local equilibrium model *Phys. Plasmas* **5** 973
[8] Jenko F, Dorland W, Kotschenreuther M and Rogers B N 2000 Electron temperature gradient driven turbulence *Phys. Plasmas* **7** 1904
[9] Xanthopoulos P and Jenko F 2006 Clebsch-type coordinates for nonlinear gyrokinetics in generic toroidal configurations *Phys. Plasmas* **13** 092301
[10] Staebler G M, Waltz R E, Candy J and Kinsey J E 2013 A new paradigm for suppression of gyrokinetic turbulence by velocity shear *Phys. Rev. Lett.* **110** 055003
[11] Candy J and Waltz R E 2003 An Eulerian gyrokinetic-Maxwell solver *J. Comput. Phys.* **186** 545
[12] Kinsey J E, Staebler G M and Waltz R E 2008 The first transport code simulations using the trapped gyro-landau-fluid model *Phys. Plasmas* **15** 055908
[13] Kinsey J E, Staebler G M, Candy J, Petty C C, Rhodes T L and Waltz R E 2015 Predictions of the near edge transport shortfall in DIII-D L-mode plasmas using the trapped gyro-Landau-fluid model *Phys. Plasmas* **22** 012507
[14] Fable E, Angioni C and Sauter O 2009 The role of ion and electron electrostatic turbulence in characterizing stationary particle transport in the core of tokamak plasmas *Plasma Phys. Control. Fusion* **52** 015007
[15] Austin M E *et al* 2019 Achievement of reactor-relevant performance in negative triangularity shape in the diii-d tokamak *Phys. Rev. Lett.* **122** 115001
[16] Staebler G M, Garofalo A M, Pan C, McClenaghan J, Van Zeeland M A and Lao L L 2018 Transport barriers in bootstrap-driven tokamaks *Phys. Plasmas* **25** 056113
[17] Garofalo A M *et al* 2015 Compatibility of internal transport barrier with steady-state operation in the high bootstrap fraction regime on DIII-D *Nucl. Fusion* **55** 123025